



Retinal capillary oximetry with visible light optical coherence tomography

Shaohua Pi^a, Tristan T. Hormel^a, Xiang Wei^a, William Cepurna^a, Bingjie Wang^a, John C. Morrison^a, and Yali Jia^{a,1}

^aCasey Eye Institute, Oregon Health & Science University, Portland, OR 97239

Edited by Akrit Sodhi, Johns Hopkins University School of Medicine, Baltimore, MD, and accepted by Editorial Board Member Jeremy Nathans April 9, 2020 (received for review October 23, 2019)

Assessing oxygen saturation (sO₂) remains challenging but is nonetheless necessary for understanding retinal metabolism. We and others previously achieved oximetry on major retinal vessels and measured the total retinal oxygen metabolic rate in rats using visible-light optical coherence tomography. Here we extend oximetry measurements to capillaries and investigate all three retinal vascular plexuses by amplifying and extracting the spectroscopic signal from each capillary segment under the guidance of optical coherence tomography (OCT) angiography. Using this approach, we measured capillary sO₂ in the retinal circulation in rats, demonstrated reproducibility of the results, validated the measurements in superficial capillaries with known perfusion pathways, and determined sO₂ responses to hypoxia and hyperoxia in the different retinal capillary beds. OCT capillary oximetry has the potential to provide new insights into the retinal circulation in the normal eye as well as in retinal vascular diseases.

capillary oximetry | visible light OCT | retinal capillary | blood oxygenation | vascular biology and physiology

The retina consists of layers of neurons and glial cells that transduce light into electrochemical impulses with which the brain produces visual cognition and perception (1). The high metabolic demand of this neurosensory tissue is supported by an intricate retinal vasculature (2) that is organized into several laminar plexuses. Abnormalities in retinal microvascular anatomy, along with alterations in the blood–retinal barrier (3) and blood flow (4), play a crucial role in various ocular diseases (5). Furthermore, alterations in blood oxygen saturation (sO₂, the fraction of oxygenated hemoglobin relative to total hemoglobin in blood vessels) are believed to be an early predictive biomarker for ocular diseases (6). Measurement of retinal sO₂, called retinal oximetry, dates back decades (7) and relies on the distinctive molar extinction coefficients of oxygenated and deoxygenated hemoglobin across a wide optical spectral range (8).

Oximetry can provide crucial insights into retinal metabolism (6), and many studies indicate the role of sO₂ in retinal pathology (9–12). However, oximetry on just retinal arteries and veins may not provide information on oxygenation of specific tissue layers or regional changes in metabolism, which may occur in some conditions, such as glaucoma, retinal vascular occlusion, or diabetic retinopathy. This will require information from individual capillary beds. Until recently, retinal capillary oximetry has remained inaccessible due to the limited spatial resolution of available imaging modalities such as fundus photography (13) and photoacoustic microscopy (14, 15). An indirect way to achieve such detail by measuring the partial pressure of oxygen (PO₂) using two-photon microscopy (16) and computing sO₂ based on the Hill equation (17) has been successfully used to measure pO₂ in cerebral capillaries (18). However, several problems limit the application of this approach to the retina. These include increased difficulty in focusing in the eye and the need to use light power that is beyond the tissue safety level (19).

Optical coherence tomography (OCT) has revolutionized ophthalmic imaging by providing detailed, depth-resolved information

on tissue structure (20). Recently, the invention of OCT angiography has enabled in vivo, noninvasive visualization of the retinal vasculature down to the capillary level (21–23), and quantitative studies have shown that alterations in retinal capillary morphology can indicate pathology earlier than changes in tissue anatomy (22). Compared to standard OCT operating in the near-infrared band, visible-light OCT (vis-OCT) (24, 25) produces higher axial resolution (26, 27) and higher spectral contrast between oxy- and deoxy-hemoglobin (8). Using vis-OCT, oximetry on major vessels in rodents and humans has been successfully demonstrated (24, 28–31) and used to monitor how progressive hypoxic challenge (32) or intraocular pressure (IOP) elevation (33, 34) affects retinal oxygen metabolism. Advances in automated detection of posterior vascular boundaries (29), acquisition of multiple circumpapillary scans (31), and quantitative quality controls (35) have been made to improve retinal oximetry on major vessels.

In this report, we describe a reliable method for measuring retinal capillary sO₂ utilizing vis-OCT. We present an in vivo assessment of hemoglobin oxygenation across the entire retinal vascular tree in rats. We also investigate the distribution of sO₂ in the different retinal vessel and capillary beds and how this responds to changes in inspired oxygen concentration.

Significance

Altered retinal metabolism contributes to neural and vascular cell apoptosis, which is implicated in many ocular diseases but is highly challenging to measure. Here we report in vivo assessment of hemoglobin oxygenation across the full vascular transition from retinal arteries to capillaries to retinal veins in rats using visible-light optical coherence tomography and demonstrate physiologic responses to alterations in the concentration of inhaled oxygen. This noninvasive technique provides access to capillary sO₂, an important factor required for determining local retinal oxygen metabolism in rodent disease models. Operating within the safety level allowed by ANSI standards for humans, this has strong potential to benefit research on ocular vascular biology and physiology and influence clinical management of patients with retinal disease.

Author contributions: S.P., J.C.M., and Y.J. designed research; S.P., X.W., and W.C. performed research; S.P., T.T.H., and X.W. contributed new reagents/analytic tools; S.P., B.W., and J.C.M. analyzed data; and S.P., T.T.H., J.C.M., and Y.J. wrote the paper.

Competing interest statement: Oregon Health & Science University and Y.J. have a significant financial interest in Optovue, Inc.

This article is a PNAS Direct Submission. A.S. is a guest editor invited by the Editorial Board.

Published under the PNAS license.

Data deposition: An additional dataset of example optical coherence tomography (OCT) and OCT angiography volumes can be found at <https://doi.org/10.6084/m9.figshare.11819982.v1>.

See online for related content such as Commentaries.

¹To whom correspondence may be addressed. Email: jjaya@ohsu.edu.

This article contains supporting information online at <https://www.pnas.org/lookup/suppl/doi:10.1073/pnas.1918546117/-DCSupplemental>.

First published May 12, 2020.

Results

Morphology of the Retinal Microcirculation in the Rat. Three laminar vascular/capillary plexuses (36)—the superficial vascular plexus (SVP), intermediate capillary plexus (ICP), and deep capillary plexus (DCP)—were projected to en face images from their respective depth slabs (Fig. 1). Compared to humans (22), retinal vascular patterns in rats are less dense and do not demonstrate radial peripapillary capillaries. Due to the much higher hemoglobin absorption of visible light, shadows underneath vessels are much darker in vis-OCT than in standard OCT. In addition, projection artifacts (37) from the SVP to deeper capillary networks, common in standard OCT, were absent in the ICP and DCP due to a stronger backscattering signal and weaker forward multiple-scattering of the visible band (27).

sO₂ measurements in major vessels can distinguish arteries (red) from veins (green) (Fig. 1E) (29). By tracing the vascular network from major vessels in en face images, arterial capillaries were found to occur predominantly in the SVP (Fig. 1B and

SI Appendix, Fig. S1), whereas veins tended to drain blood from the DCP (Fig. 1D and SI Appendix, Fig. S1) (36). Within the SVP, we noted few direct connections between arteries and veins, making it possible to classify capillaries in this layer, by whether they were connected to arteries or veins (Figs. 1B and 2). For the purpose of analyzing sO₂, we designated these capillaries as either arterial or venous since we thought that their responses might differ from each other. A similar capillary designation was not possible for the ICP and DCP capillaries, since these were less discrete than the SVP. As capillary segments of ICP appeared to terminate frequently in the en face image, the ICP was suggested to serve as a bridging plexus between the SVP and DCP in the rat retina.

As the three laminar vascular plexuses are located parallel to each other but in different retinal layers, vertical interplexus capillaries are essential to form a connected network. Since interplexus capillaries are perpendicular to the retinal layers and have greater absorption length along the direction of light illumination,

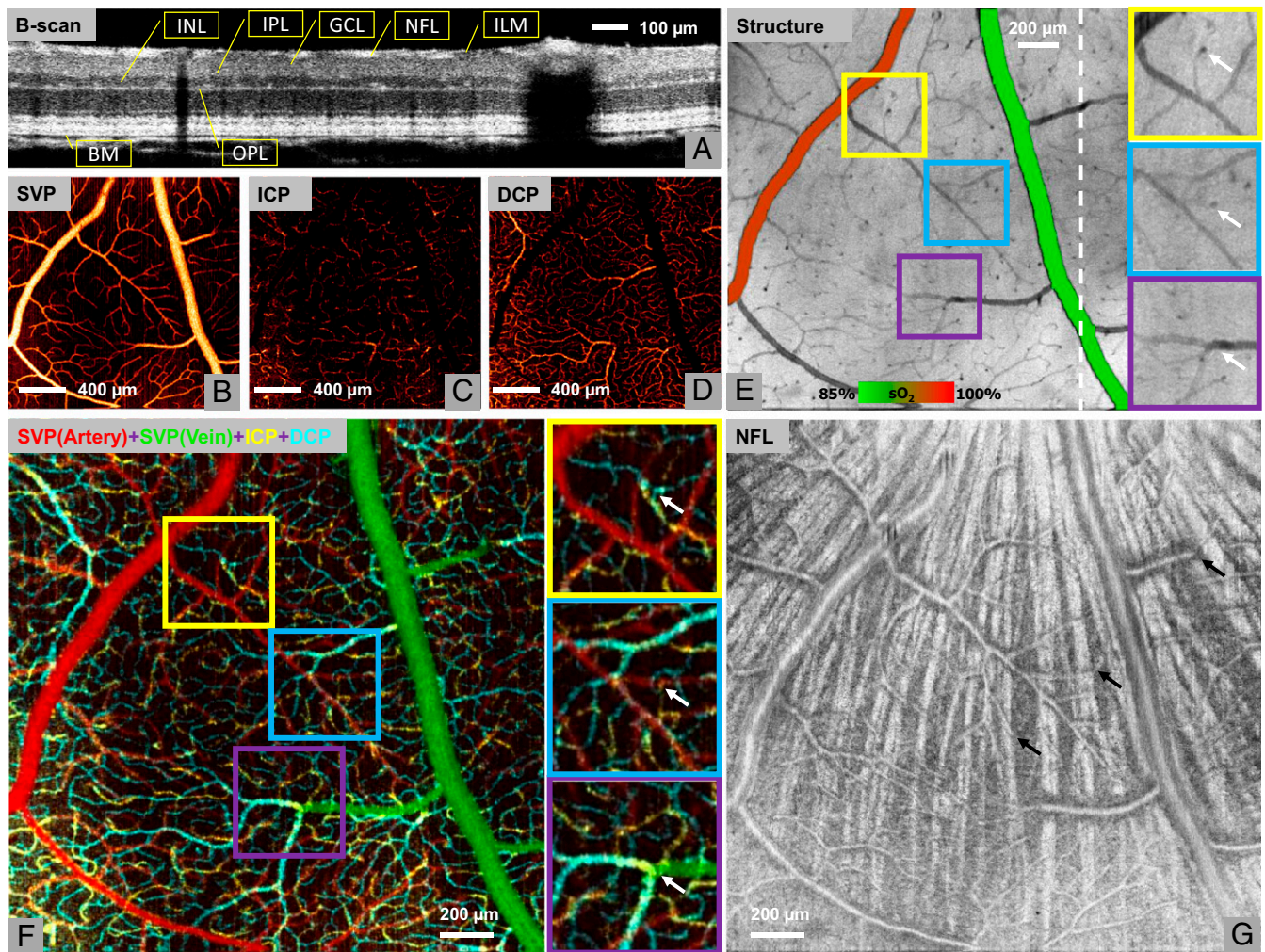


Fig. 1. (A) B-scan image of a brown Norway rat retina using visible-light OCT. NFL, nerve fiber layer; GCL, ganglion cell layer; IPL, inner plexiform layer; INL, inner nuclear layer; OPL, outer plexiform layer; BM, Bruch's membrane. (B–D) En face images of vascular/capillary plexuses. SVP projected in the NFL and GCL slabs. ICP projected in the slab containing the inner border of the INL. DCP projected in the slab containing the outer border of the INL. (E) En face structural image projected from the ILM to BM, overlaid with measured oxygen saturation (sO₂) values in major vessels in order to differentiate arteries from veins in an animal breathing 100% O₂. Interplexus capillaries (white arrows) appear as dark spots due to greater light absorption than neighboring capillaries. (F) Overlaid en face angiograms of three vascular/capillary plexuses to demonstrate the detailed organization of the retinal circulation. Examples of interplexus capillaries (indicated by white arrows in the enlarged images) were validated by observing their presence in corresponding locations. (G) En face projection of the NFL slab. The SVP was found to run anterior to the nerve fiber bundles (bright radial striations), which appear posterior to the vessels. The interplexus capillaries (black arrows) penetrate between NFL bundles and connect the SVP to the ICP and DCP.

they appeared as dark spots in structural en face OCT (Fig. 1E). Interplexus capillaries were further identified by observing their presence in overlaid en face angiograms of the three vascular/capillary plexuses (Fig. 1F). These interplexus capillaries were frequently found at the distal ends (turning points to deeper plexuses) of superficial capillaries, as well as in some bifurcations (SI Appendix, Fig. S1).

Owing to the high resolution of vis-OCT, the nerve fiber bundles could be clearly visualized in en face images by projecting the structural reflectance signal in the nerve fiber layer (Fig. 1G). They appeared as bright radial striations running from the retinal periphery toward the optic disk. Gaps between the nerve fiber bundles gradually tapered as the fibers coalesced while approaching the optic nerve head. The SVP can be visualized anterior to the nerve fiber bundles in the en face image, with interplexus capillaries penetrating gaps between bundles (Fig. 1G and SI Appendix, Fig. S2).

Retinal Microcirculatory sO₂. Using the algorithm described in *Methods*, the sO₂ in retinal capillaries, as well as that in retinal arteries and veins, could be measured in vivo. The sO₂ in major vessels was similar to that reported earlier (24, 29, 32), with corresponding levels in capillaries. sO₂ of major vessels as well as capillaries was noted to change in response to changes in inspired O₂ (Fig. 2). The sO₂ results between two measurement sessions (Fig. 3A) in each plexus at all conditions were repeatable, as shown by a Bland–Altman analysis (SI Appendix, Fig. S3). The mean difference between measured sO₂ in two sessions

was $0.2 \pm 2.6\%$, with a Pearson correlation coefficient of 0.96 (P value < 0.01). The interscan repeatability (pooled SD) was calculated as 1.9% of absolute sO₂.

The measured retinal arterial sO₂ correlated well with the systemic sO₂, and the sO₂ in veins was lower than that in arteries (Fig. 3B). The averaged sO₂ values in the SVP capillaries connected to arteries (SVP-AC), ICP capillaries, and DCP capillaries were all similar, and all were lower than that in arteries (Fig. 3B). Distinctively, venous sO₂ could be lower or higher than capillary sO₂, depending on the inhalation conditions. In addition, the sO₂ in SVP capillaries connected to veins (SVP-VC) was different from the values in other capillaries, possibly due to the extensive presence of large-caliber venules, which may function more like retinal veins (Fig. 3C).

To investigate the distribution of sO₂ along perfusion paths more specifically, we examined the levels of sO₂ by capillary order in SVP arterial capillaries, in which successive tributaries of capillaries arising from larger arterial vessels could be easily traced. The capillary order was determined by the abundance of branches in the network (*Methods*). First-order capillaries, which might in fact be arterioles, were directly connected with retinal arteries and had a larger caliber than their downstream vessels. sO₂ in these vessels was closer to the values in retinal arteries than that of successive capillary orders (Fig. 3D). At progressively higher orders, the caliber of capillary segments decreased, and perfusion distance increased (*Methods*). Overall, sO₂ decreased gradually with increasing capillary order (Fig. 3D), consistent with a release of oxygen to tissues along these capillaries. In fifth-order

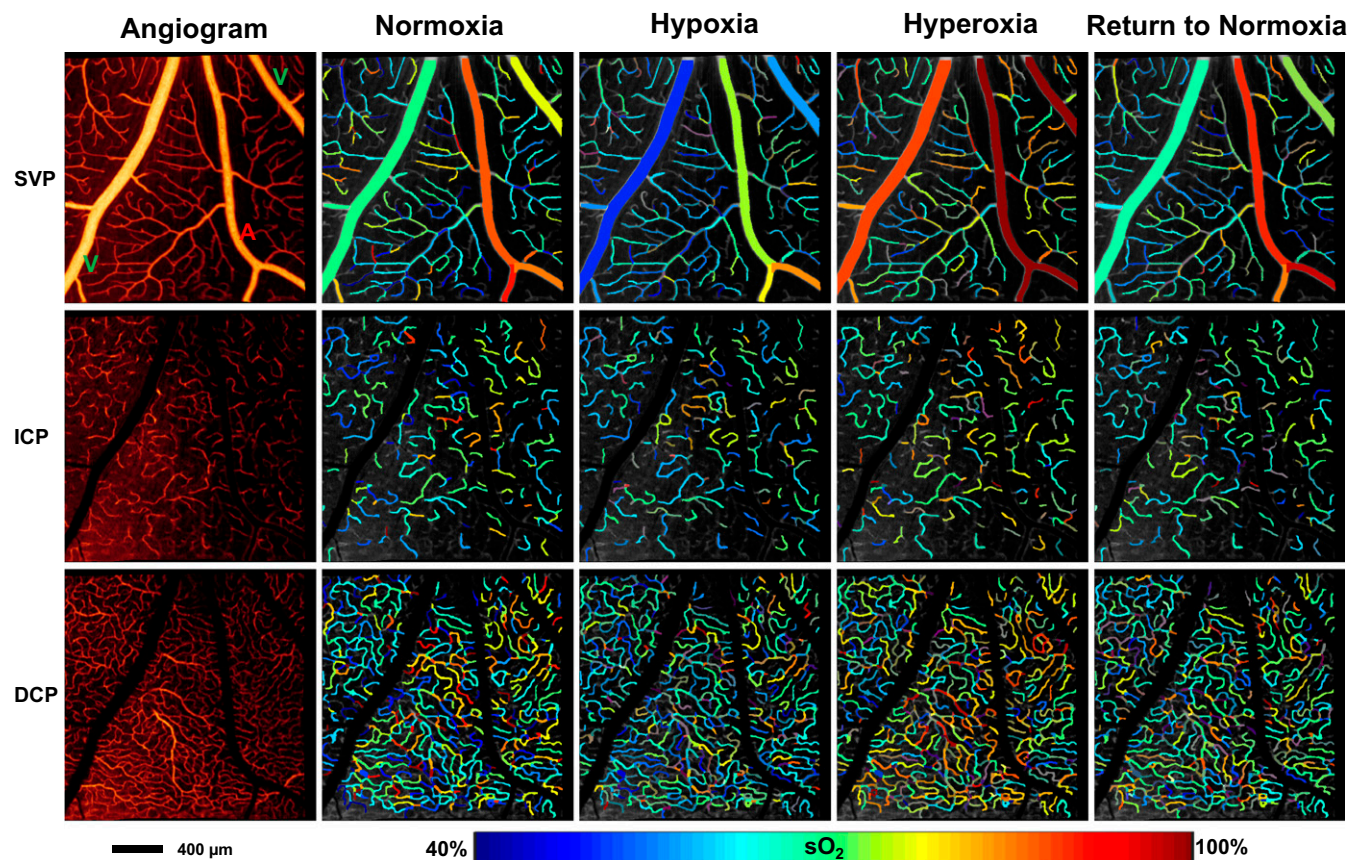


Fig. 2. Representative capillary sO₂ along with that in major vessels (A, artery; V, vein) in one rat retina responding to regulation in oxygen concentration in inhaled gas, from 21% (normoxia) to 15% (hypoxia), then to 100% (hyperoxia) and to 21% (return to normoxia). The angiogram (2 × 2 mm) was obtained by averaging all eight scans at all conditions acquired in the same region. The sO₂ in capillary segments corresponded to trends shown by the sO₂ in major vessels, which decreased with the reduction of oxygen concentration in the inhaled gas.

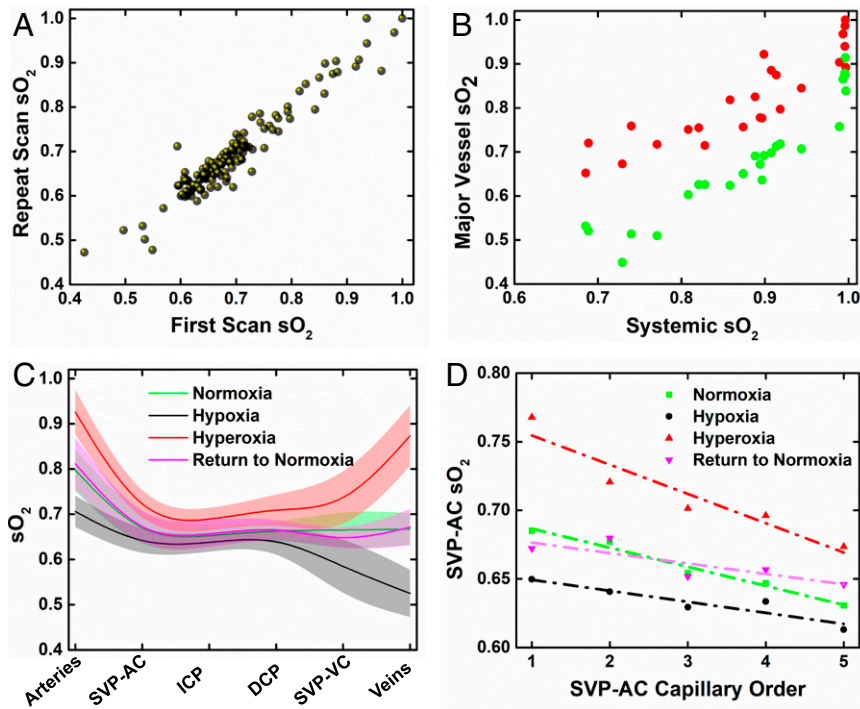


Fig. 3. Statistics of changes in vascular sO_2 with inhaled oxygen concentration, from normoxia to hypoxia, then to hyperoxia and return to normoxia. (A) The relationship between the averaged sO_2 in each plexus between the first session and second session indicated good repeatability of capillary oximetry. (B) Correlation of major vessel sO_2 with changes in systemic arterial sO_2 , which decreased in hypoxia and increased in hyperoxia, as compared to normoxia. Data point symbol colors indicate arteries (red) and veins (green). (C) The mean \pm SD of sO_2 in retinal arteries, SVP arterial capillaries (SVP-AC), ICP capillaries, DCP capillaries, SVP venous capillaries (SVP-VC), and retinal veins for each concentration of inspired oxygen. (D) The SVP-AC sO_2 decreased with increasing capillary order, indicating oxygen delivery along these capillaries.

capillaries, sO_2 was maintained at almost the same level as that in the ICP and DCP. As expected, increased capillary perfusion distance, which was positively correlated with capillary order, was associated with a decrease in sO_2 (SI Appendix, Fig. S4).

Retinal Microcirculatory sO_2 Responses to Hypoxia/Hyperoxia. Overall, sO_2 in the retinal circulation decreased during hypoxia, increased during hyperoxia, and returned to normal when conditions returned to normoxia (Figs. 2 and 3C). However, the extent of these responses was not identical in the different plexuses. Venous sO_2 changed most dramatically (Fig. 3B and C) from a low of $52.5 \pm 5.7\%$ in hypoxia to a high of $85.3 \pm 6.0\%$ in hyperoxia. The oxygen extraction, calculated as the difference between arterial and venous sO_2 , was $\sim 20\%$ in normoxia and hypoxia and reduced to $\sim 14\%$ in hyperoxia.

Compared to the sO_2 in major vessels, the sO_2 in capillaries changed less during inhaled oxygen regulation. For the SVP arterial capillaries, ICP capillaries, and DCP capillaries, the absolute value of sO_2 decreased by $\sim 2\%$ (P value < 0.01) in hypoxia and increased by $\sim 4\%$ (P value < 0.01) in hyperoxia, as compared to an sO_2 of $\sim 65\%$ in normoxia.

Discussion

Assessing capillary oxygen saturation is desirable but challenging. First, as the spectral contrast from absorption increases with the vertical propagation of light into deeper retinal layers, capillaries become much harder to identify due to their small caliber and reduced accumulation of spectral contrast. Second, there are fewer blood cells than in major vessels, and their passage is intermittent, leading to a discrete, stochastic signal (38). Finally, it is difficult to accurately determine the axial location of each capillary. Previously, oxygen saturation in major retinal vessels was achieved by us (29) and other groups (24, 28, 31). The possibility

of performing capillary oximetry by spectral contrast using a backscattering-based image modality like OCT has been demonstrated through numerical simulations (39) and was recently achieved using dual-band, dual-scan inverse spectroscopic OCT in the mouse ear (40). However, capillary oximetry in the retina is more challenging, given the optical aberrations presented by the eye and more strict safety limitation on laser illumination in the eye than in other tissue. In this work, the ultrahigh resolution of vis-OCT allowed us to visualize the three vascular plexuses in the retinal circulation clearly, as well as individual nerve fiber bundles, which has not been possible previously without using adaptive optics to correct for aberrations (41). We achieved retinal capillary oximetry by effectively extracting the spectroscopic signal from each capillary segment. As can be seen in Fig. 2, sO_2 values can be obtained from almost all capillary segments. The failure of capillary oximetry, which occurred on only $\sim 2\%$ capillary segments, was mainly due to problems with posterior vessel border detection. As expected (42, 43), transient sO_2 fluctuations in capillaries, associated with the random passage of individual erythrocytes, were observed between capillary segments and within individual segments between scans. The reliability of the algorithm was supported by good interscan repeatability and demonstration of an expected reduction in sO_2 along SVP capillaries with known perfusion pathways.

Capillaries are the major site of O_2 delivery to local tissue. Given this, reduced sO_2 along the blood flow path would be anticipated. We found that capillary sO_2 decreases with increasing capillary order within the SVP for arterial capillaries, consistent with decreased oxygen pressure (PO_2) observed by two-photon microscopy in cerebral blood circulation (18). These findings suggest that oxygen delivery is occurring along capillaries in the SVP. Interestingly, we did not observe further changes in sO_2 between fifth-order capillaries and those of the

ICP and DCP. The significance of this finding at present is uncertain as the anatomic relationships between the ICP and DCP capillary beds are complicated and not fully understood. Further work using this technology is warranted to help clarify the role of the ICP and DCP in delivering oxygen to the deeper layers of the retina.

We recognize that capillary sO_2 is not a direct measure of local tissue ischemia. However, this can be used to calculate tissue oxygenation. Since retinal tissue oxygen is supplied by diffusion from capillaries, one can first convert measured sO_2 to oxygen pressure in the capillaries using the oxygen-hemoglobin dissociation curve and then, from this, calculate oxygen diffusion from capillaries to the retinal tissue using Fick's law (*Methods*). The resulting calculation reveals distinct levels of tissue oxygen pressure in different layers of the retina (*SI Appendix, Fig. S9*) in a pattern that strongly parallels a published axial profile of tissue oxygen pressure measured by invasive oxygen-sensitive microelectrodes in the rat (6). This not only demonstrates that tissue oxygenation can be derived from capillary sO_2 , it illustrates that capillary sO_2 can provide level-specific information on retinal oxygenation. This could be particularly valuable in diseases where some layers of the retina are preferentially damaged, as in glaucoma, which primarily affects the nerve fiber layer and retinal ganglion cells and in which inner retinal capillary dropout has been documented (44).

In this initial model, each capillary plexus was simplified to a single-layer diffusion source, which limits calculated diffusion to the axial dimension. In future refinements, we will resolve the true three-dimensional (3D) positions of each vessel (demonstrated in *SI Appendix, Fig. S5*), allowing us to locate them as diffusion sources of oxygen. From the locations of these vessels in three dimensions we can determine lateral as well as axial diffusion. In this manner, measurements of capillary sO_2 will lead to noninvasive generation of 3D retinal tissue maps of oxygen pressure. This may be particularly valuable in vaso-occlusive diseases, such as diabetes and vascular occlusion, which may result in local reductions in tissue oxygenation or potentially, as in the case of retinal vein occlusion, increases in postcapillary venules produced by bypass via collateral vessels.

As expected, systemic sO_2 and that in major retinal arteries and veins varied in parallel with the concentration of inspired O_2 . However, we found relatively small changes in retinal capillary sO_2 under conditions of hypoxia and hyperoxia. Although we have not confirmed this in our own animals using an alternative method, reports using microelectrodes have noted a similarly muted response in oxygen tension to hyperoxia in the inner 50% of the rat retina (45, 46), which, as shown in *SI Appendix, Fig. S9*, corresponds to the SVP, ICP, and DCP. Interestingly, long-term oxygen exposure in rabbits, which lack this control, can produce severe retinal degeneration (47). Our results, obtained in young adult animals, likely reflect the ability of a healthy retinal microcirculation to maintain a stable source of oxygen delivery when challenged by changing systemic oxygen conditions. Studies using the current technique, along with further refinements described here, will be needed using animal models of retinal disease to test their validity. In the case of chronic models, this may require using physiologic challenge experiments, such as varying inspired oxygen, as used here, or acute IOP elevation (33). These will help uncover underlying mechanistic changes, such as impaired autoregulation, that may otherwise be obscured by compensatory mechanisms.

We also found that while sO_2 in veins was equivalent to that in capillaries when exposed to normoxic conditions, this increased and was higher than that in capillaries in hyperoxia. As suggested by other studies (18, 48), this might be due to the discrepancy between the length-weighted mean capillary sO_2 (the calculated averaged capillary sO_2 in this study) and the flow-weighted mean capillary sO_2 (closer to sO_2 in veins). In this situation, capillaries

with faster flow (which would tend to have a higher oxygen saturation due to less oxygen extraction along their path) might contribute more blood to the veins. Testing this, as well as understanding how autoregulation contributes to the control of inner retinal oxygen tension in hyperoxia, will require the ability to measure blood velocity in individual capillary segments. We believe that this is possible with further optimization of the vis-OCT algorithm, and efforts to achieve this are currently underway.

Limitations exist for this study. First, our approach requires averaging over frames. Thus, the temporal resolution in some cases may be insufficient to capture transient changes in oxygen saturation and oxygen metabolism. Second, it must be remembered that sO_2 is measured using visible light as the illumination source. As this in itself may induce microvascular responses through neurovascular coupling (49, 50), measurements may in part reflect the sO_2 of an active, responding nervous system. Work will be needed with normal subjects as well as disease models in order to understand better the impact of this influence. Third, to reduce discomfort (as may accompany photoreceptor bleaching) during retinal imaging in awake humans, using a lower-power illumination (<0.22 mW) (26, 30) than the American National Standards Institute (ANSI) laser safety standard may be more clinically acceptable. This may in turn affect image quality and measurements of capillary sO_2 . Because the human eye has a longer focal length than the rat, the light beam at the pupil would need to be enlarged for retinal imaging in humans in order to maintain the same lateral resolution. While the current instrument provides a $20^\circ \times 20^\circ$ field of view, significantly wider fields can be obtained by post-processing, as shown in *SI Appendix, Fig. S1C*. Fourth, this technique does not yet provide velocimetric data for individual capillary segments. However, as mentioned above, we believe that this will be possible with further refinements in vis-OCT. Since blood flow velocity in conjunction with sO_2 determines the oxygen transport rate within specific vessels, this information, applied to 3D capillary maps, can be used to determine regional changes in oxygen metabolism in specific tissue beds. The vis-OCT capillary oximetry method demonstrated here is an important step in achieving this capability.

In summary, we have acquired high-resolution, 3D images of rodent retinas with vis-OCT and calculated sO_2 along capillary segments by fitting their respective spectroscopic signals. In contrast to the human retina (51), we found that the SVP runs anterior to the nerve fiber bundles and that the interplexus capillaries penetrate the gaps between nerve fibers to connect with the ICP and DCP. From en face angiograms of the vascular plexuses, we determined the perfusion pathway, length, centerline, and normal directions of capillary segments in the SVP and further quantified the perfusion distance and order for arterial capillaries in this layer. We achieved retinal capillary oximetry in the three vascular plexuses in the rat retina and further described the sO_2 distribution pattern along the blood flow transition pathway from major retinal arteries to major retinal veins, as well as the physiological responses to hypoxic and hyperoxic conditions. Use of this technology and its expansion to determine 3D tissue maps of oxygenation along with velocimetry will help to clarify and expand our understanding of the retinal oxygen supply in health and disease.

Methods

Animal Preparation. Six wild-type brown Norway rats (14 wk old) were included in this study. The animals were initially anesthetized with 5% isoflurane in a sealed box for 10 min, followed by 2.5% isoflurane mixed with inhalation gas during imaging. After anesthesia, the animal was immobilized in a custom-made imaging stage with multidimensional manipulation for alignment. The right eyes of animals were selected for imaging, yielding a total of six eyes for statistical analysis. The pupil was dilated with a 1% tropicamide ophthalmic solution before imaging. To keep the cornea moisturized, sterile irrigating salt solution (Alcon Laboratories Inc.) was applied to the eye every other minute. The animal's body temperature was maintained at 38.5°C using a water-warming blanket. The exhaust gas was

removed by a vacuum pump to avoid carbon dioxide and excess isoflurane accumulation and collected by an anesthesia gas filter (OMNICON F/air, Bickford) before releasing to the open air.

During imaging, the oxygen concentration in the inhalation gas was regulated from normoxia (21% O₂), to hypoxia (15% O₂), to hyperoxia (100% O₂), and returned to normoxia. Oxygen regulation was achieved by changing the ratio of the pure oxygen, normal air, and nitrogen with the total gas flow rate maintained at ~1 L/min, with oxygen concentration monitored by a calibrated oxygen analyzer (MiniOX I; Ohio Medical Corporation). The systemic arterial oxy-hemoglobin saturation (SaO₂), respiration rate, and pulse were recorded by a pulse oximeter (MouseOx Plus; STARR) attached to the left rear paw of the animal. In general, the respiratory rate was ~45 breaths per minute in normoxia, increased to ~70 in hypoxia and decreased to ~35 in hyperoxia. For each condition, the animal was allowed to rest for 3 to 5 min, and imaged only after the SaO₂ reading stabilized. In general, the animal was maintained at each condition for about 6 min. All observations were completed for each animal in about 30 min.

All experimental procedures were approved by the Institutional Review Board/Ethics Committee and the Institutional Animal Care and Use Committee of the Oregon Health & Science University (OHSU).

OCT Image Acquisition. The vis-OCT used here is a custom-built prototype (27) housed in the Center for Ophthalmic Optics & Lasers laboratory of OHSU's Casey Eye Institute. The illumination spectrum covered the high-absorption contrast region of hemoglobin from 510 to 610 nm ($\lambda_c = 560$ nm; full width at half maximum was ~90 nm) and was calibrated with a neon calibration light source (NE-1; Ocean Optics). The dispersion mismatch between the two arms was compensated both physically and numerically. An unbalanced 90:10 wideband fiber optical coupler delivered 10% power into the sample arm (power = 0.8 mW, which is within the safety level of laser power allowed by ANSI standards). A telescope tube ($f_1 = 75$ mm, $f_2 = 11$ mm) guided light into the eye. The system operated at a flexible axial scan sampling rate and scanning angle, with a 1.2- μ m axial resolution and ~6- μ m lateral resolution with an image depth of 1.8 mm. The maximum sensitivity was measured as 89 dB with a protected silver mirror.

Two repeated volumetric raster scans were collected near the optic disk with a field of view of 2 × 2 mm at each inhalation condition. Each scan consisted of 512 axial profiles in the fast transverse scanning direction to form a B scan, with three repeated B scans at each slow transverse scanning direction and 512 slow transverse scanning positions. The acquisition for each volumetric scan was completed within 17 s at a sampling rate of 50 kHz. The recorded interferogram was processed for OCT structure, and the split-spectrum amplitude-decorrelation angiography (SSADA) algorithm (52) was used for OCT angiography. Layer segmentation was done with a graph-

search technique (53) on structural B-scan images. The laminar vascular/capillary plexuses were then generated by projecting the flow signal within specific slabs. Registration (54) was performed for en face images at all conditions acquired at the same region, and the images were then averaged to improve the signal-to-noise ratio.

Capillary Segment Extraction. Using en face OCT angiograms (Fig. 4A) from each vascular plexus, vessel binary masks (Fig. 4B) were obtained by thresholding frangi-vesselness-filter enhanced angiograms. Six binary masks were created for each eye (36), including four in the SVP for retinal arteries, capillaries connected to arteries (SVP-AC in Results), capillaries connected to veins (SVP-VC in Results), and retinal veins, as well as two for capillaries in the ICP and DCP. All binary masks were skeletonized (Fig. 4C) using a thinning algorithm to delineate the vascular centerline, collapsing vascular caliber information and preserving only the connectivity. The vascular points in the skeleton were further differentiated as vascular end points, body points, bifurcation points, and overlay points by counting the number of neighboring vascular pixels N. Specifically, the capillary end points had only N = 1 neighboring point, body points had N = 2 neighboring points, bifurcation points had N = 3, and overlay points had N greater than or equal to 4.

To extract capillary segments, all bifurcation and overlay points (red dots in Fig. 4C) were removed from the skeleton. The capillary segments were then isolated from each other (capillary segment, green text in Fig. 4D), with the coordinates of the centerline read from the image (red scatter line in Fig. 4D). Based on the coordinates, capillary normal directions (yellow arrows in Fig. 4D), capillary segment length, and capillary orientation could be determined. Together with vessel binary masks (Fig. 4B), capillary segment binary masks and capillary calibers could also be determined. It should be noted that the capillary segmentation could also be performed volumetrically prior to retinal layer segmentation (SI Appendix, Fig. S5).

Posterior Capillary Border Detection. After extracting capillary segments (Fig. 5A), a series of reconstructed B scans (Fig. 5B) were resampled on both the structural and angiographic volumes along the capillary normal directions, with the transverse positions centered on the centerline. Before resampling, the original B scans were first aligned according to the center of mass of the averaged axial profile to reduce the effect of animal motion. After that, the reconstructed B scans were registered to one reference frame (we used the middle frame in each capillary segment). The shifts in each A line were recorded for later spectroscopic processing. All registered structural and angiographic B scans along the capillary segment were then averaged to extract the capillary anterior and posterior borders described below (Fig. 5C).

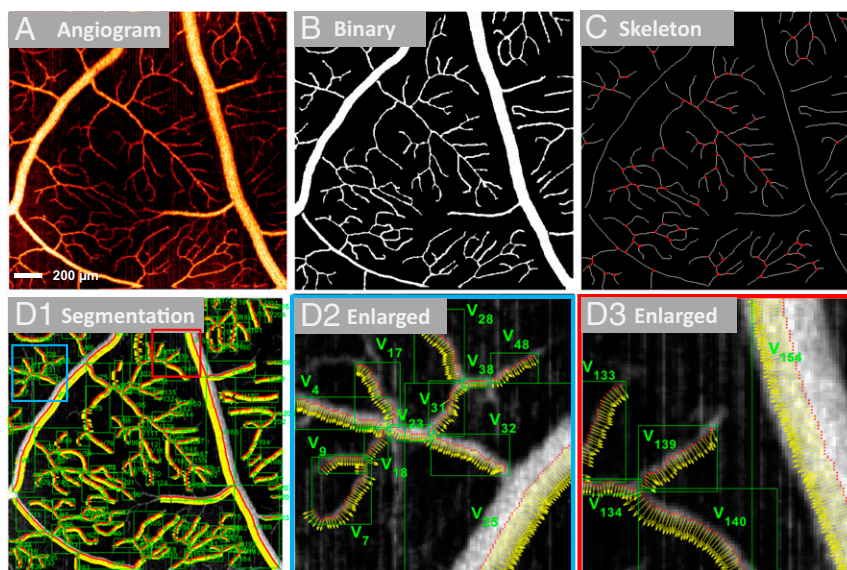


Fig. 4. Illustration of capillary segment extraction. (A) En face angiogram (2 × 2 mm) showing the SVP. (B) Vascular binary mask obtained by thresholding the enhanced angiogram. (C) The skeleton showing vascular centerlines. The detected bifurcation and overlay points are marked by red dots. (D1–D3) All detected capillary segments in the scanned field of view (D1) labeled with vascular segment sequence number (green text), region (green boxes), and normal direction (yellow arrows). Enlarged, detailed views corresponding to the blue and red boxes in D1 are shown in D2 and D3, respectively.

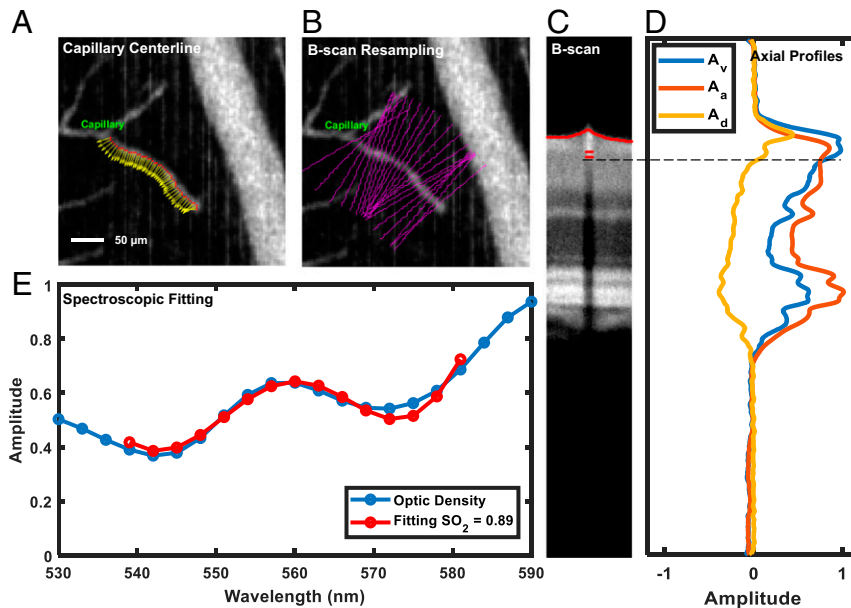


Fig. 5. Illustration of oximetry processing on a capillary segment. (A) Normal directions (yellow arrows) were extracted along the detected capillary centerline (red). (B) B scans were resampled along the normal directions of the capillary segment (magenta lines). (C) The resampled B scans were registered and averaged to localize the posterior border (red) of the capillary. (D) The averaged vessel reflectance axial profile (A_v) and averaged reflectance axial profile of the entire B scan (A_a), along with their difference (A_d), can identify the vessel posterior border (black dashed line) by the zero-crossing depth of the difference profile A_d . (E) Capillary sO_2 was derived by a spectroscopic fitting (red) to the detected spectrum (blue).

The merged angiographic and structural B scans were then flattened to the inner limiting membrane (ILM) boundaries (red line in Fig. 5C) for further processing. Since the reconstructed B scans were resampled along the capillary segment and averaged, the signal from other capillaries and noise were largely suppressed while only the signal from the specific capillary segment of interest was enhanced. The anterior border of the capillary segment was determined by the first suprathreshold voxel in the averaged capillary angiogram axial profile. Usually, vascular voxels have stronger reflectance and larger decorrelation values (due to the scattering of red blood cells) than neighboring tissues, whereas the voxels underneath vascular pixels have much lower reflectance than neighboring tissues due to severe absorption of hemoglobin in the visible light range. The posterior border (black dashed line in Fig. 5D) of the capillary segment was obtained by finding the zero-crossing position in the reflectance difference axial profile (A_d) of the averaged vessel reflectance axial profile (A_v) and the averaged reflectance axial profile for the entire B-scan (A_a) (Fig. 5D). In summary, the posterior segment

identification process, the detailed steps of which appear in *SI Appendix, Fig. S6*, was accomplished by comparing the structural and angiographic axial profiles in capillaries with their neighboring tissues. This method was found to work consistently for vessels of different diameters (*SI Appendix, Fig. S7*).

Spectroscopic Fitting. The spatial- and depth-resolved optical density $OD(z, \lambda)$ in the capillary (blue line in Fig. 5E) is defined as the logarithm of the ratio for reflected intensity spectrum $I(z, \lambda)$ to the source spectrum $I_0(\lambda)$. It stands for the reflectivity of the tissue and is determined by extinction coefficients based on a modified Beer's law:

$$OD(z, \lambda) = \ln\left(\frac{I(z, \lambda)}{I_0(\lambda)}\right) = -2(z - z_0)[C_{HbO_2} \epsilon_{HbO_2}(\lambda) + C_{Hb} \epsilon_{Hb}(\lambda)] - \alpha \ln(\lambda) + \ln(AR_0). \quad [1]$$

Here z_0 and z are the depth of anterior and posterior voxels, respectively, and $z - z_0$ is the accumulated absorption length for the vessels. The scattering

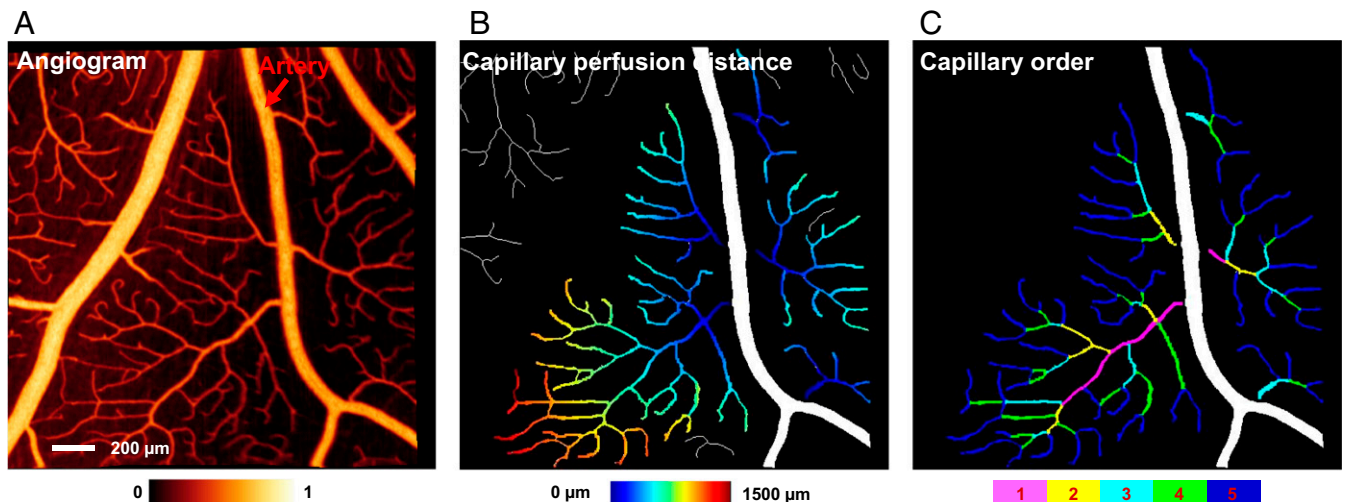


Fig. 6. (A) The angiogram of SVP, as well as (B) the capillary perfusion distances map and (C) capillary order for the SVP arterial capillaries.

spectrum of the vessel wall $r(\lambda)$ was modeled as a power law $A \cdot \lambda^{-\alpha}$ under the first-order Born approximation (55). The scattering spectrum at the reference arm R_0 was considered as a wavelength-independent constant. The subscripts HbO_2 and Hb indicate the contribution from oxygenated and deoxygenated hemoglobin, respectively, with their extinction coefficients ϵ referring to literature values (8) and concentrations C being calculated by fitting, in order to find the oxygen saturation $sO_2 = C_{HbO_2} / (C_{HbO_2} + C_{Hb})$.

Optical density $OD(z, \lambda)$ was extracted by a short-time Fourier transform spectroscopic analysis of the interference fringes (Fig. 5E). A Gaussian window with a full width at half maximum of ~ 9 nm and an interval distance around 3 nm were applied, resulting in 21 split spectra bands in total. Only those bands within the contrast region from 527 to 582 nm were selected for linear regression fitting for the sO_2 .

Capillary Bed Morphology. The SVC capillary perfusion distance, which was defined as the shortest distance between a capillary segment to a major vessel through the vascular network (Fig. 6), was quantified by using the weighted shortest-path problem model (56). Specifically, the identified capillary segments were assigned as nodes in the model, and the identified bifurcation points were used to construct a connection graph for their capillary segments. The weight of each connection channel P_{ij} was defined as the mean capillary lengths for the i th and j th capillary segments. After obtaining the perfusion distance, node lists of the shortest pathways were also recorded. It should be noted that the capillary perfusion distance for some capillary segments (marked white in Fig. 6B) could not be obtained due to the limited field of view.

By establishing the shortest pathways for all capillary segments to reach a major vessel, we could determine the primary connections along the network. The parent and children branch segments in bifurcations could be determined by comparing their perfusion distances. The upstream and downstream segments for each capillary segment were also determined by the recorded node lists in the shortest pathways, revealing the flow directions of each capillary segment (SI Appendix, Fig. S8). After that, the pixel-wised capillary perfusion distance maps were generated by gradually increasing the distance along the flow direction (Fig. 6B).

SVC capillary order was further quantified for each capillary segment by counting downstream segments (SI Appendix, Fig. S8). As shown in Fig. 6C, the capillary segments were determined as first-order (count larger than 20, magenta, which may represent arterioles), second-order (count between 19 and 8, yellow), third-order (count between 7 and 3, cyan), and fourth-order (count between 2 and 1, green) capillary segments. The capillary segments without a downstream capillary segment were identified as fifth-order capillary segments (count 0, blue).

Calculation of Retinal Oxygen Pressure Profile from Capillary sO_2 . The oxygen demand of retinal tissue is satisfied by the oxygen diffusion from four capillary plexuses, i.e., the SVP, the ICP, the DCP, and the choriocapillaris, where the oxygen pressure (PO_2) can be calculated from the sO_2 values through the oxy-hemoglobin dissociation curve (SI Appendix, Fig. S9A) (57). As the choroid is a highly vascularized tissue, the PO_2 in the choriocapillaris is assumed to be similar to that in retinal arteries and is obtained from the averaged sO_2 in the retinal arteries. Since the retina consists of layers that differ in axial direction, the diffusion can be simplified to a one-dimensional process and described using the second-order Fick's law (6, 32, 58, 59) as below:

$$Q_i = DK \frac{d^2 P_i}{dx^2} \quad P_i(x) = \frac{Q_i}{2DK} x^2 + \alpha_i x + \beta_i, \quad [2]$$

where Q is oxygen consumption in the layer, D is oxygen diffusivity ($1.97 \times 10^{-5} \text{ cm}^2/\text{s}$), k is to oxygen solubility coefficients [$2.4 \text{ mL O}_2/(\text{mL retina} \cdot \text{mmHg})$], with x (μm) the depth of retina and $P(x)$ the PO_2 at that depth. The subscript i indicates the specific slab. Based on the relative depth of four capillary plexuses to these two layers, we could model the retina into six slabs (SI Appendix, Fig. S9B), which are the nerve fiber layer and ganglion cell layer (slab 1), the inner plexiform layer (slab 2), the inner nuclear layer and outer plexiform layer (slab 3), the outer nuclear layer (slab 4), the photoreceptor inner segments (slab 5), and the photoreceptor outer segments and retinal pigment epithelium (slab 6). According to a previous study (59), the majority of oxygen consumption is in the inner plexiform layer for the inner retina and in the photoreceptor inner segments for the outer retina. Thus, the Q_1 , Q_3 , Q_4 , and Q_6 are considered negligible and set to 0 for slabs 1, 3, 4, and 6. By solving the diffusion equation we can model the PO_2 profile at each slab (Eq. 2). By applying the boundary conditions at the four capillaries plexuses and other interface of slabs, the $\alpha_i \sim \alpha_6$, and $\beta_1 \sim \beta_6$ are obtained to calculate the PO_2 along the depth of retina.

Data Availability. All relevant data have been included within the manuscript and SI Appendix. An additional dataset of example OCT and OCT angiography volumes can be found at <https://doi.org/10.6084/m9.figshare.11819982.v1>.

ACKNOWLEDGMENTS. This work was supported by grants R01 EY027833, R01 EY024544, R01 EY010145, and P30 EY010572 from the National Institutes of Health (Bethesda, MD) and an unrestricted departmental funding grant and William & Mary Greve Special Scholar Award from Research to Prevent Blindness (New York, NY).

1. A. P. Schachat, C. P. Wilkinson, D. R. Hinton, S. R. Sadda, P. Wiedemann, *Ryan's Retina E-Book*, (Elsevier Health Sciences, 2017).
2. H. R. Zhang, Scanning electron-microscopic study of corrosion casts on retinal and choroidal angioarchitecture in man and animals. *Prog. Retin. Eye Res.* **13**, 243–270 (1994).
3. J. Cunha-Vaz, *The Blood-Retinal Barriers*, (Springer Science & Business Media, 2013), Vol. 32.
4. C. J. Pournaras, E. Rungger-Brändle, C. E. Riva, S. H. Hardarson, E. Stefansson, Regulation of retinal blood flow in health and disease. *Prog. Retin. Eye Res.* **27**, 284–330 (2008).
5. L. P. Aiello *et al.*, Vascular endothelial growth factor in ocular fluid of patients with diabetic retinopathy and other retinal disorders. *N. Engl. J. Med.* **331**, 1480–1487 (1994).
6. R. A. Linsenmeier, H. F. Zhang, Retinal oxygen: From animals to humans. *Prog. Retin. Eye Res.* **58**, 115–151 (2017).
7. A. Harris, R. B. Dinn, L. Kagemann, E. Rechtman, A review of methods for human retinal oximetry. *Ophthalmic Surg. Lasers Imaging* **34**, 152–164 (2003).
8. N. Bosschaert, G. J. Edelman, M. C. Aalders, T. G. van Leeuwen, D. J. Faber, A literature review and novel theoretical approach on the optical properties of whole blood. *Lasers Med. Sci.* **29**, 453–479 (2014).
9. R. F. Gariano, T. W. Gardner, Retinal angiogenesis in development and disease. *Nature* **438**, 960–966 (2005).
10. M. Hammer *et al.*, Diabetic patients with retinopathy show increased retinal venous oxygen saturation. *Graefes Arch. Clin. Exp. Ophthalmol.* **247**, 1025–1030 (2009).
11. S. H. Hardarson, E. Stefansson, Retinal oxygen saturation is altered in diabetic retinopathy. *Br. J. Ophthalmol.* **96**, 560–563 (2012).
12. R. Heitmar, S. Safeen, Regional differences in oxygen saturation in retinal arterioles and venules. *Graefes Arch. Clin. Exp. Ophthalmol.* **250**, 1429–1434 (2012).
13. M. Hammer, W. Vilser, T. Riemer, D. Schweitzer, Retinal vessel oximetry-calibration, compensation for vessel diameter and fundus pigmentation, and reproducibility. *J. Biomed. Opt.* **13**, 54015 (2008).
14. H. F. Zhang, K. Maslov, G. Stoica, L. V. Wang, Functional photoacoustic microscopy for high-resolution and noninvasive in vivo imaging. *Nat. Biotechnol.* **24**, 848–851 (2006).
15. S. Jiao *et al.*, Photoacoustic ophthalmoscopy for in vivo retinal imaging. *Opt. Express* **18**, 3967–3972 (2010).
16. S. Sakadžić *et al.*, Two-photon high-resolution measurement of partial pressure of oxygen in cerebral vasculature and tissue. *Nat. Methods* **7**, 755–759 (2010).
17. K. Uchida, M. P. Reilly, T. Asakura, Molecular stability and function of mouse hemoglobins. *Zool. Sci.* **15**, 703–707 (1998).
18. S. Sakadžić *et al.*, Large arteriolar component of oxygen delivery implies a safe margin of oxygen supply to cerebral tissue. *Nat. Commun.* **5**, 5734 (2014).
19. P. T. So, C. Y. Dong, B. R. Masters, K. M. Berland, Two-photon excitation fluorescence microscopy. *Annu. Rev. Biomed. Eng.* **2**, 399–429 (2000).
20. D. Huang *et al.*, Optical coherence tomography. *Science* **254**, 1178–1181 (1991).
21. Y. Jia *et al.*, Quantitative optical coherence tomography angiography of vascular abnormalities in the living human eye. *Proc. Natl. Acad. Sci. U.S.A.* **112**, E2395–E2402 (2015).
22. A. H. Kashani *et al.*, Optical coherence tomography angiography: A comprehensive review of current methods and clinical applications. *Prog. Retin. Eye Res.* **60**, 66–100 (2017).
23. R. F. Spaide, J. G. Fujimoto, N. K. Waheed, S. R. Sadda, G. Staurengi, Optical coherence tomography angiography. *Prog. Retin. Eye Res.* **64**, 1–55 (2018).
24. J. Yi, Q. Wei, W. Liu, V. Backman, H. F. Zhang, Visible-light optical coherence tomography for retinal oximetry. *Opt. Lett.* **38**, 1796–1798 (2013).
25. X. Shu, L. Beckmann, H. Zhang, Visible-light optical coherence tomography: A review. *J. Biomed. Opt.* **22**, 1–14 (2017).
26. T. Zhang, A. M. Kho, V. J. Srinivasan, Improving visible light OCT of the human retina with rapid spectral shaping and axial tracking. *Biomed. Opt. Express* **10**, 2918–2931 (2019).
27. S. Pi *et al.*, Angiographic and structural imaging using high axial resolution fiber-based visible-light OCT. *Biomed. Opt. Express* **8**, 4595–4608 (2017).
28. S. P. Chong, C. W. Merkle, C. Leahy, H. Radhakrishnan, V. J. Srinivasan, Quantitative microvascular hemoglobin mapping using visible light spectroscopic Optical Coherence Tomography. *Biomed. Opt. Express* **6**, 1429–1450 (2015).
29. S. Pi *et al.*, Automated spectroscopic retinal imaging with visible-light optical coherence tomography. *Biomed. Opt. Express* **9**, 2056–2067 (2018).
30. S. Chen *et al.*, Retinal oximetry in humans using visible-light optical coherence tomography [Invited]. *Biomed. Opt. Express* **8**, 1415–1429 (2017).

31. B. T. Soetikno, L. Beckmann, X. Zhang, A. A. Fawzi, H. F. Zhang, Visible-light optical coherence tomography oximetry based on circumpapillary scan and graph-search segmentation. *Biomed. Opt. Express* **9**, 3640–3652 (2018).
32. J. Yi *et al.*, Visible light optical coherence tomography measures retinal oxygen metabolic response to systemic oxygenation. *Light Sci. Appl.* **4**, e334 (2015).
33. S. Pi *et al.*, Monitoring retinal responses to acute intraocular pressure elevation in rats with visible light optical coherence tomography. *Neurophotonics* **6**, 41104 (2019).
34. W. Song *et al.*, Longitudinal detection of retinal alterations by visible and near-infrared optical coherence tomography in a dexamethasone-induced ocular hypertension mouse model. *Neurophotonics* **6**, 41103 (2019).
35. R. Liu, W. Song, V. Backman, J. Yi, Quantitative quality-control metrics for *in vivo* oximetry in small vessels by visible light optical coherence tomography angiography. *Biomed. Opt. Express* **10**, 465–486 (2019).
36. S. Pi *et al.*, Rodent retinal circulation organization and oxygen metabolism revealed by visible-light optical coherence tomography. *Biomed. Opt. Express* **9**, 5851–5862 (2018).
37. R. F. Spaide, J. G. Fujimoto, N. K. Waheed, Image artifacts in optical coherence angiography. *Retina* **35**, 2163–2180 (2015).
38. B. Li *et al.*, Two-photon microscopic imaging of capillary red blood cell flux in mouse brain reveals vulnerability of cerebral white matter to hypoperfusion. *J. Cereb. Blood Flow Metab.* **40**, 501–512 (2020).
39. R. Liu *et al.*, Theoretical model for optical oximetry at the capillary level: Exploring hemoglobin oxygen saturation through backscattering of single red blood cells. *J. Biomed. Opt.* **22**, 25002 (2017).
40. R. Liu *et al.*, Single capillary oximetry and tissue ultrastructural sensing by dual-band dual-scan inverse spectroscopic optical coherence tomography. *Light Sci. Appl.* **7**, 57 (2018).
41. Y. Jian *et al.*, Wavefront sensorless adaptive optics optical coherence tomography for *in vivo* retinal imaging in mice. *Biomed. Opt. Express* **5**, 547–559 (2014).
42. D. G. Lyons, A. Parpaleix, M. Roche, S. Charpak, Mapping oxygen concentration in the awake mouse brain. *eLife* **5**, e12024 (2016).
43. A. S. Golub, R. N. Pittman, Erythrocyte-associated transients in PO₂ revealed in capillaries of rat mesentery. *Am. J. Physiol. Heart Circ. Physiol.* **288**, H2735–H2743 (2005).
44. A. Chen *et al.*, Measuring glaucomatous focal perfusion loss in the peripapillary retina using OCT angiography. *Ophthalmology* **127**, 484–491 (2020).
45. S. J. Cringle, D.-Y. Yu, Regulation of oxygen tension in the mammalian retina during systemic hyperoxia is species dependent. *Adv. Exp. Med. Biol.* **1072**, 241–244 (2018).
46. S. J. Cringle, D.-Y. Yu, A multi-layer model of retinal oxygen supply and consumption helps explain the muted rise in inner retinal PO₂ during systemic hyperoxia. *Comp. Biochem. Physiol. A Mol. Integr. Physiol.* **132**, 61–66 (2002).
47. G. H. Bresnick, Oxygen-induced visual cell degeneration in the rabbit. *Invest. Ophthalmol.* **9**, 372–387 (1970).
48. A. G. Tsai, P. C. Johnson, M. Intaglietta, Oxygen gradients in the microcirculation. *Physiol. Rev.* **83**, 933–963 (2003).
49. A. Mishra, A. Hamid, E. A. Newman, Oxygen modulation of neurovascular coupling in the retina. *Proc. Natl. Acad. Sci. U.S.A.* **108**, 17827–17831 (2011).
50. M. R. Metea, E. A. Newman, Glial cells dilate and constrict blood vessels: A mechanism of neurovascular coupling. *J. Neurosci.* **26**, 2862–2870 (2006).
51. Z. Liu, K. Kurokawa, F. Zhang, J. J. Lee, D. T. Miller, Imaging and quantifying ganglion cells and other transparent neurons in the living human retina. *Proc. Natl. Acad. Sci. U.S.A.* **114**, 12803–12808 (2017).
52. Y. Jia *et al.*, Split-spectrum amplitude-decorrelation angiography with optical coherence tomography. *Opt. Express* **20**, 4710–4725 (2012).
53. M. Zhang *et al.*, Advanced image processing for optical coherence tomographic angiography of macular diseases. *Biomed. Opt. Express* **6**, 4661–4675 (2015).
54. S. Pi *et al.*, Imaging retinal structures at cellular-level resolution by visible-light optical coherence tomography. *Opt. Lett.* **45**, 2107–2110 (2020).
55. J. Yi, V. Backman, Imaging a full set of optical scattering properties of biological tissue by inverse spectroscopic optical coherence tomography. *Opt. Lett.* **37**, 4443–4445 (2012).
56. E. W. Dijkstra, A note on two problems in connexion with graphs. *Numer. Math.* **1**, 269–271 (1959).
57. J. W. Severinghaus, Simple, accurate equations for human blood O₂ dissociation computations. *J. Appl. Physiol.* **46**, 599–602 (1979).
58. J. C. Lau, R. A. Linsenmeier, Oxygen consumption and distribution in the Long-Evans rat retina. *Exp. Eye Res.* **102**, 50–58 (2012).
59. S. J. Cringle, D.-Y. Yu, P. K. Yu, E.-N. Su, Intraretinal oxygen consumption in the rat *in vivo*. *Invest. Ophthalmol. Vis. Sci.* **43**, 1922–1927 (2002).